INTERNATIONAL JOURNAL OF AUTOMOTIVE AND MECHANICAL ENGINEERING (IJAME)
ISSN: 2229-8649 e-ISSN: 2180-1606
VOL. 19, ISSUE 3, 9872 – 9891
DOI: https://doi.org/10.15282/ijame.19.3.2022.01.0761

ORIGINAL ARTICLE

Drag Reduction on a Three-Dimensional Teardrop-Shaped Body Car with Different Stagnation Points

M.W. Lee, H.S.K. Tiew, W.S. Chang, M.H.H. Ishak and Farzad Ismail*

School of Aerospace Engineering, Engineering Campus, Universiti Sains Malaysia, 14300 Pulau Pinang, Malaysia

ABSTRACT – The long-term goal in the automotive industry is to reduce fuel consumption and environmental pollution without compromising the aerodynamic performance of the car. Herein, the aerodynamic performance of an in-house designed Shell Eco-Marathon prototype car is analyzed using Computational Fluid Dynamics simulations. Shape optimization of the Shell car is executed to reduce drag by modifying the rear underbody profile and stagnation point position. The effect of one modification to another is studied to determine the changes to overall flow around the car and, more importantly, the lift and drag coefficients. It has been found that the stagnation point height has a higher influence on the aerodynamic performance of the car compared to variations of the rear underbody, with optimum drag reductions of 17% and 10%, respectively. Moreover, combining the two best configurations to the car reduces CD by 25%, and this marks the highest drag reduction achieved in this study.

ARTICLE HISTORY
Received: 27th Jan. 2022
Revised: 1st June 2022
Accepted: 30th June 2022
Published: 30th Sept 2022

KEYWORDS
Teardrop shape;
Car aerodynamic;
Computational fluid;
Dynamic

INTRODUCTION

The quest for energy saving in the automobile industry is crucial to alleviate the energy crisis and help in reducing environmental issues. These two global problems require multi-faceted solutions from different fields of research. One of the prevailing topics is the fuel efficiency of a car, which can be enhanced by improving the powertrain, aerodynamic shape and material type. The Shell Eco-Marathon is a competition where the student teams compete to build a car with the greatest fuel efficiency. The focus herein would be to improve its aerodynamic performance through shape modifications. However, the aerodynamic analysis of the external flow of road vehicles is challenging since the flow around a car is three-dimensional with salient features including flow separation, formation of vortices and unsteady wake. These salient features, coupled with the nature of complicated geometry of a moving car, lead to complex turbulent flows especially in the rear end. The work presented by Guilmineau [1] shows the computational study on the Ahmed body by employing RANS model, where the numerical results showed good agreement with the experiment except for the flow reattachment. Besides that, CFD simulation was performed on the Ahmed body to study the interaction between vortex structures and the rear window at the near wake [2].

Many drag reduction methods have been developed to enhance the aerodynamic performance of road vehicles to reduce their fuel consumption. The underbody of a racing car was sliced to increase streamlining, hence delaying the flow separation behind the car body [3]. The simulation results reported a 22% of drag reduction when applying a sliced rear under-body. Moreover, the work presented by Sirenko et al. [4] showed a drag reduction of about 26% due to fairing being attached at the back of a car to reduce the wake region. Several CFD works have been done by previous teams to investigate the aerodynamic characteristics of Shell Eco-Marathon Car. The work presented by CifljDski et al. [5] proposed several shape recommendations for a prototype car based on the model used in the previous competition to improve the aerodynamic performance. About 70% of drag reduction was achieved by carrying out modifications on the front nose, underneath and rear part of the car. Model iterations were carried out to improve the aerodynamic coefficients by modifying the fairing, and changing car yaw angle and wheel tilt angle [6].

There are several studies that attempted to explore the aerodynamic performance around vehicles. Ravelli and Savini [7] studied the aerodynamics of an F1 car by using a numerical method. They used an open-source CFD code (OpenFOAM) to evaluate the performance of racing car in terms of drag, front balance and efficiency. Thabet and Thabit [8] examined the flow characteristics over a model car (Ahmed body) with a slant angle of 40°. They compared their numerical results with the available experimental data. They found out that the numerical results well agreed with experimental data. Recently, Haffner et al. [9] focused on the turbulent wake mechanism of bluff body drag (Ahmed body). They discovered that the recirculation intensity was increased by the large flow in the recirculation region. Their experimental results also showed solutions to address the wake flow which leads to drag reduction. The aerodynamics behavior of Ahmed body is studied numerically [10]. Their results demonstrated that the effect of pressure generated at the back of body (wake flow) could increase the drag of the whole body. Furthermore, they also demonstrated the flow pattern at the wake region, which is useful to determine the resistance and fuel efficiency.

Further wind tunnel measurements were made for the well-defined and simplified geometries, such as the Windsor body [11], Asmo body [12], or Ahmed body without rear slant [13]. It is concluded that when the wheel is added to the

*CORRESPONDING AUTHOR | Farzad Ismail | ✉ aefarzad@usm.my

base model, an upwash-dominated wake was formed that results in loss of vertical symmetry [11]. The major wake areas for heavy vehicles are between the rear end regions and wheels. The drag created for rear end could be reduced by using boat tails [14]. Their results show that the performance of a robust drag reduction is interrupted under moderate cross-wind conditions, particularly when compared with a curved cavity. On bluff bodies, a study was done on the modified bus model to reduce the aerodynamic drag by using ANSYS [15]. Their numerical results show about 30% drag reduction after modifications have been done to the bus.

Few studies have used various turbulent models to investigate the aerodynamic performance of vehicles' surroundings. Huang et al. [16] utilized Large Eddy Simulation (LES) to simulate large-scale turbulent motion at the entrance structure of the forecabin in an Ahmed body. Compared to the original Ahmed model, the presence of the forecabin will increase the oscillation frequency of the flow field by approximately 15 times. Lastly, it appears that the high drag coefficient moment is always caused by the production of a more complicated or strong vortex motion. An Arbitrary Hybrid Turbulence Modeling (AHTM) was developed by Maulenkul et al. [17] using a combination of Reynolds Averaged Navier-Stokes (RANS), Unsteady Reynolds Averaged Navier-Stokes (URANS), Large Eddy Simulation (LES), and Direct Numerical Simulation (DNS) turbulence models in a single flow field based on the local mesh refinement. When compared to the traditional benchmark case of an Ahmed body, their findings indicated that the ATHM is the most precise of all turbulent models.

Recently, there have been growing demands for electric and solar vehicles to have more aerodynamic efficiency. Although there was an attempt to realize a new design inspired by a boxfish [18], but currently the trend is toward a teardrop shape. The teardrop shape is pulling more attention in the automotive industry and is already applied in the new electric concept cars, such as Toyota i-TRIL and Persu V3. The teardrop shape is proposed herein as a baseline model to maximize the aerodynamic efficiency. However, the CFD analysis of aerodynamic characteristics around a teardrop-shaped car is scant. To the authors' best knowledge, no research has been concentrated on investigating the teardrop shape in a thorough manner, especially the wake flow of the teardrop shape. Without an in-depth study, teardrop-shaped vehicles might have high drag while travelling at average or normal speeds. Furthermore, very few studies are focused on the aerodynamic optimization of different sections of a teardrop-shaped car and the effect of one modification to another. This paper aims to perform an analysis on the aerodynamic performance of a fully-assembled Shell Eco-Marathon prototype car with a teardrop shape to determine its optimal aerodynamics efficiency, ensuring the saving of energy, thus solving the problems faced previously. The shape optimization is done on different parts of the car body, including the nose and rear underbody. In addition, the influence of one modification on another is analyzed to determine the aerodynamics contribution from the different body parts.

METHODOLOGY

Geometrical Modelling for Ahmed Body Benchmark

The orthogonal view of the Ahmed body and the control volume (refer to Figure 2 in [19]) created around it with the respective dimensions are shown in Figure 1 and Figure 2. Half of Ahmed body is simulated to reduce the computational cost since the flow is assumed to be symmetric. Several volumetric limit size boxes are created in the main control volume to allow a higher degree of freedom in controlling the mesh and limit the mesh size in the different regions around the car. The mesh was locally refined in regions that are important, especially in the wake region and underbody region, while the coarser mesh is used at less relevant places to reduce the computational cost with just a sufficient number of grids to predict the physics correctly. Prism layers are applied near the Ahmed body and road to capture the boundary layer flow. The growing prism inflation layer option has been implemented on the wing boundaries with the first adjacent cell above the wall set at 0.0001m with 20 layers in a growth rate set to 1.108.

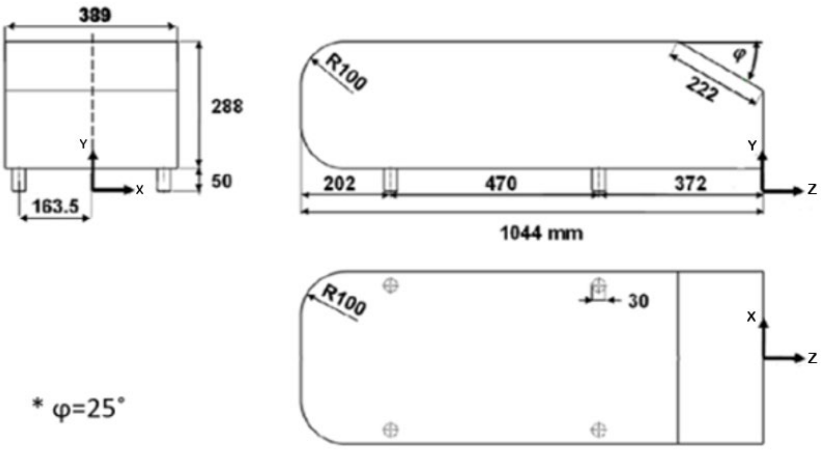

Figure 1. Dimensions of Ahmed Body.

Prototype Car

The proposed car model is designed based on a teardrop shape, combining two aerofoils NACA 66012 and NACA 0012, into one body, as shown in Figure 2. The teardrop shape is modified to provide the required internal space for a single driver while possibly maintaining its streamlined shape. There are two flow conditions for the prototype car, one with $Re=4.29\times10^6$ to compare its performance with Ahmed body while $Re=1.33\times10^6$ is used to simulate the actual driving conditions. The overview and parameters of the Shell car are shown in Figure 3 and Figure 4. It is worth mentioning that relatively the same domain, control volume and mesh sizes used in Ahmed body simulation are applied to the prototype Shell car simulation.

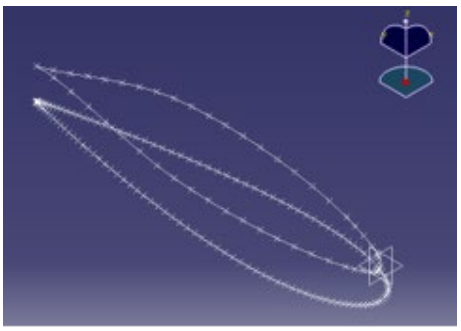

Figure 2. Combination of two airfoils.

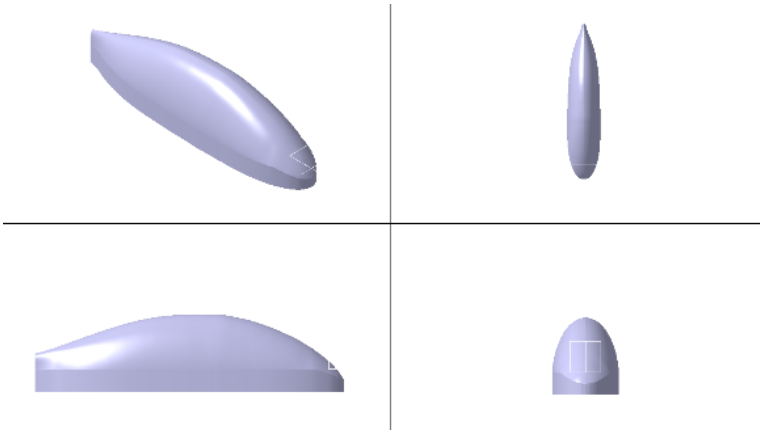

Figure 3. Prototype car design.

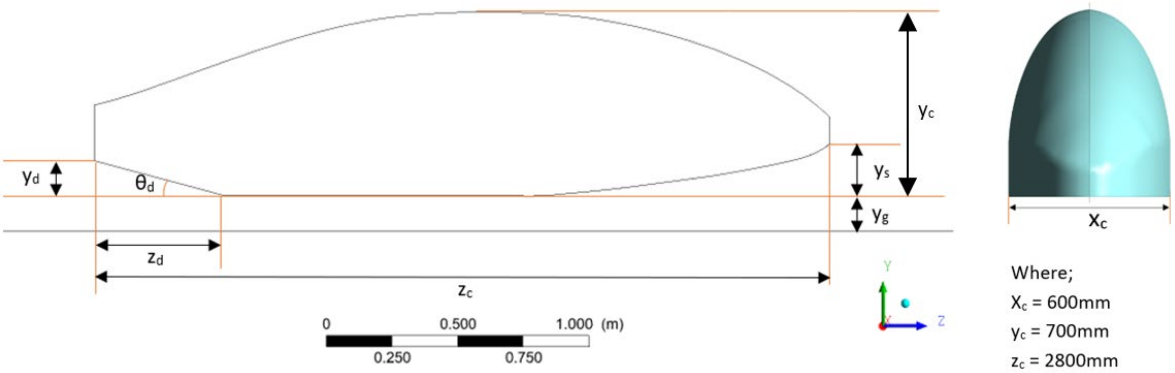

Figure 4. Parameters of Shell car.

The car body will be assembled with other components, including chassis, wheel and fairing, as shown in Figure 5. The aerodynamic performance of the fully assembled car will be analyzed to provide more realistic results. External components are expected to have higher influences on aerodynamic performance. The influence of each component on the aerodynamic performance will be investigated.

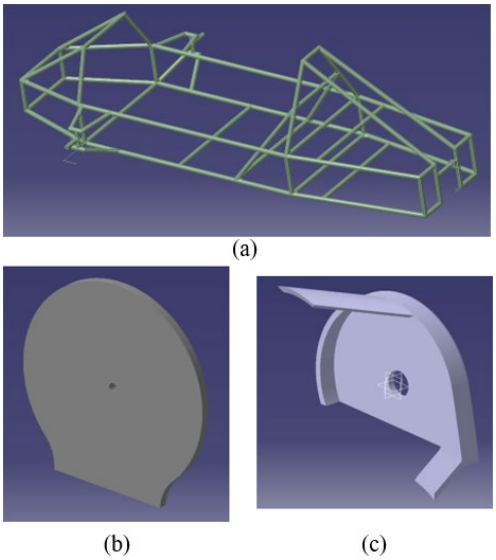

Figure 5. Simplified version of (a) chassis, (b) wheel and (c) fairing.

Computational Modelling

The flow herein satisfies the incompressible Navier-Stokes (NS) equation with turbulent flow, and is solved through the Reynolds-Averaged Navier-Stokes (RANS) equations. Using Einstein notation in Cartesian coordinates, the continuity is given by

$$\frac{\partial u_i}{\partial x_i} = 0, \tag{1}$$

where u_i denotes the fluids velocity in index form. The momentum equation is,

$$\frac{\partial (u_i\, u_j)}{\partial x_j} = -\frac{1}{\rho}\frac{\partial P}{\partial x_i} + g_i + \nu \frac{\partial}{\partial x_j}\left(\frac{\partial u_i}{\partial x_j} + \frac{\partial u_j}{\partial x_i}\right) \tag{2}$$

where P is the pressure acting on the fluids, g_i denotes the gravitational field strength which only appears in the negative y direction, followed by the shear stress tensor on the fluids due to the viscous effects. The viscosity ν contains both the physical and eddy viscosities of which the latter is obtained via Menter's SST k-ω/ k-ε model [20].

Turbulence Kinetic Energy, k:

$$\frac{\partial}{\partial t}(\rho k) + \frac{\partial}{\partial x_i}(\rho k u_i) = \frac{\partial}{\partial x_j}\left(\Gamma_k \frac{\partial k}{\partial x_j}\right) + \tilde{G}_k - Y_k + S_k, \tag{3}$$

Specific dissipation rate, ω:

$$\frac{\partial}{\partial t}(\rho \omega) + \frac{\partial}{\partial x_i}(\rho \omega u_i) = \frac{\partial}{\partial x_j}\left(\Gamma_\omega \frac{\partial \omega}{\partial x_j}\right) + G_\omega - Y_\omega + D_\omega + S_\omega \tag{4}$$

where Γ_k and Γ_ω are effective diffusivity of k and ω, respectively, $\tilde{G}_k$ is generation of turbulence kinetic energy due to mean velocity gradients, G_ω is generation of ω, Y_k and Y_ω are dissipation of k and ω respectively, S_k and S_ω are user-defined source terms, , and D_ω is cross-diffusion term. Accurate calculations in the near-wall region with high solution gradients are important to the success of the boundary layers simulation, where SST k-ω turbulence models (Eq. 3-4) are combined with the viscous sublayer formulation, and the logarithmic layer formulation is based on y+<1. The details and implementations of Eq. 3-4 can be found therein [20].

To maintain the continuity equation, the momentum equation is solved together with a pressure Poisson equation given by

$$\frac{\partial^2 P}{\partial x_j \partial x_j} = -\frac{1}{\rho}\frac{\partial}{\partial x_j}\left(u_j \frac{\partial u_i}{\partial x_j}\right), \tag{5}$$

which is solved iteratively using the coupled method. The momentum equation is numerically solved using a second-order upwind finite volume method with an implicit time integration technique. Second-order Least-Squares Cell-Based gradients and second-order pressure schemes are also used herein.

Boundary Condition

A uniform airflow with Reynolds number of 4.29×10^6 enters the inlet, while the flow exits the outlet at atmospheric pressure conditions, as shown in Figure 6. Note that the pressure herein is based on relative pressure to the standard atmospheric pressure (gauge pressure). The boundary conditions for the faces of cars and domains are stationary wall with non-slip condition. The Shear-Stress Transport k-ω model is used since it gives a smaller error in predicting the drag coefficient compared to the k-epsilon model [21].

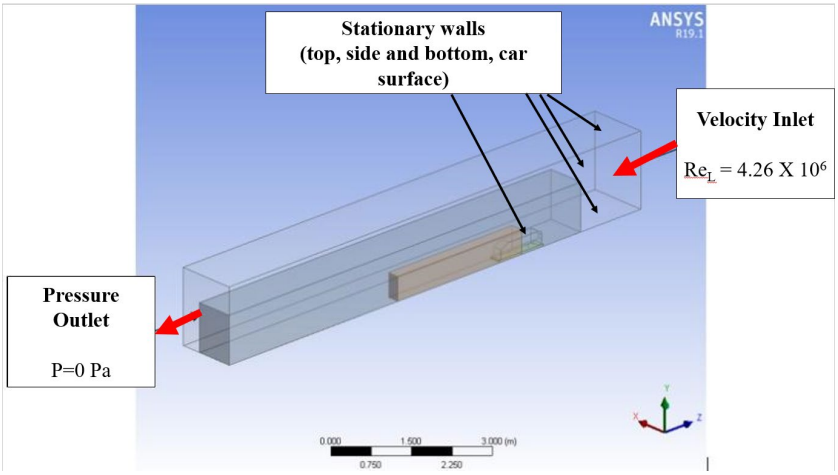

Figure 6. Boundary condition for car simulation.

Grid Independence Test (GIT)

Grid independence tests are carried out by using 1 million (1M), 1.5M, 2M, 4M, 6M and 8.5M of element numbers to select the suitable mesh to simulate the flow around both the Ahmed body and Shelll car. The result of GIT is shown in Figure 7 and 6.35M number of elements is selected as a trade of between the accuracy and computational costs. The computational mesh of Ahmed body simulation is shown in Figure 8. Mesh metrics for 3D non-uniform grid are checked to ensure that the mesh is qualified based on the mesh quality recommended by [22] and [23] as shown in Table 1. Y-plus requirement is shown in Table 2.

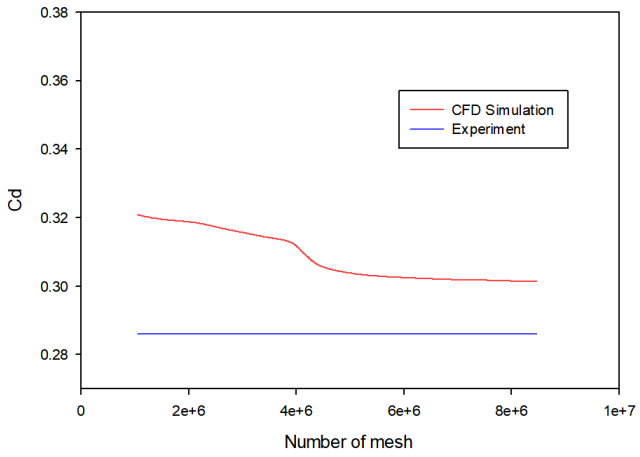

Figure 7. Result of grid independence test for Ahmed Body in comparison to experiment data [24].

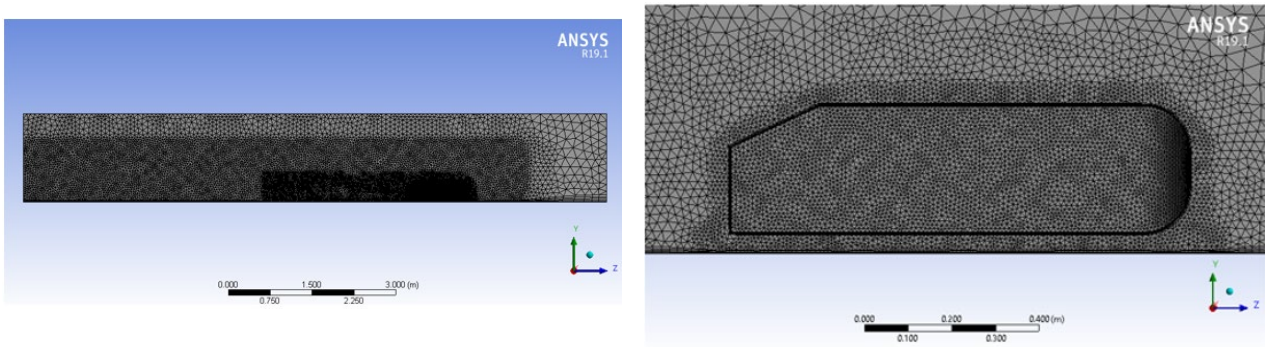

(a) (b)

Figure 8. Mesh of Ahmed body in (a) overall view and (b) zoom-in view.

Table 1. Mesh quality.

	Aspect ratio			Skewness		
	Requirement	Ahmed body	Shell Car	Requirement	Ahmed body	Shell Car
Min	-	1.671	1.1792	-	2.7663×10^{-4}	1.0339×10^{-3}
Max	-	22.509	21.675	0.9	0.88619	0.7079
Avg	20	2.0015	1.912	0~0.2	0.14053	0.12737

Table 2. Y-plus values.

Turbulence model	Requirement	Ahmed body	Shell Car
K-ω	y+ <5	9<y+<287	8<y+<40

The influence of y+ with different numerical model on the shape optimization was also studied in order to reduce the numerical error at the regions that are prone to flow separation and wall.

Table 3. Comparison table for different types of meshes in terms of Y+ values.

Mesh	SST k-ω		K-Epsilon	
	Y^+ Min	Y^+ Max	Y^+ Min	Y^+ Max
1001254	11.85	37.57	11.85	37.57
2014563	9.07	29.16	9.07	29.16
4000653	5.78	20.38	4.96	20.38
6356663	2.38	11.12	0.25	13.04
8456392	0.56	6.32	0.16	4.32

Based on Table 3, the most optimum results were found with a number mesh of 6.35 Million for the SST k-ω. The Y^+ value for the buffer layer has a range of $1< Y^+<10$. Thus, SST k-ω model was considered the optimum model for this type of flow geometry.

After the Ahmed body simulation is established, the Grid independence tests for shell eco car are carried out by using 1 million (1M), 1.5M, 2M, 4M, 6M and 8.5M of element numbers. The computational mesh of shell car body simulation is shown in Figure 9. Figure 10 depicts the outcome of GIT, and 6M elements were chosen as a compromise between accuracy and processing costs.

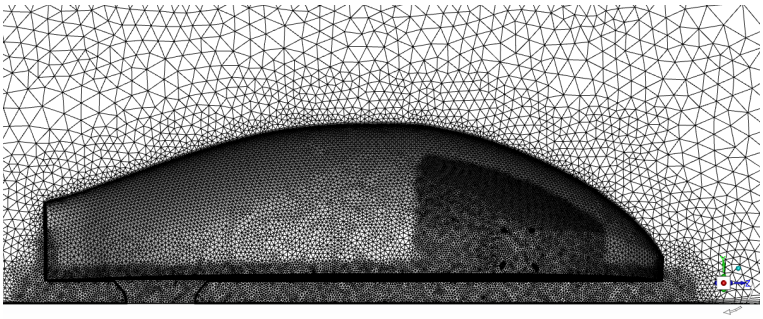

Figure 9. Mesh of shell car body in zoom-in view

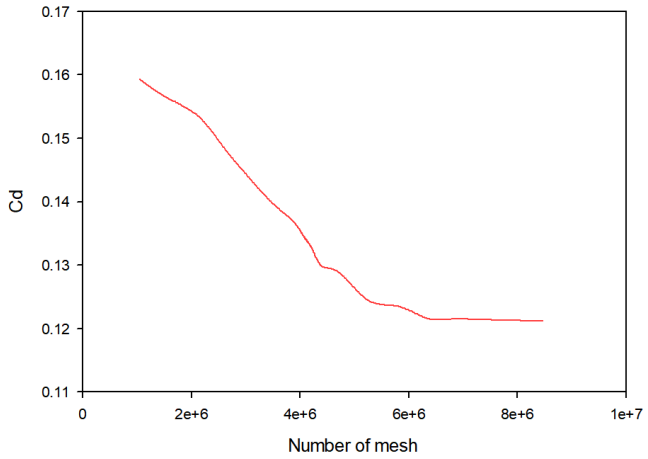

Figure 10. Result of grid independence test for Shell Eco car.

VALIDATION

Quantitative: Drag Coefficient

The predicted drag coefficient of Ahmed body is compared to the experimental data obtained from the literature [24]. Three different turbulence models were simulated and the results were compared to determine the most suitable turbulence model, which was similarly done by Abdullah et al. [25]. Based on Table 4, k-ω has the highest accuracy in predicting the drag of Ahmed body as there is only about 6% difference between the simulation and experimental results. SA model is the least accurate because of the low capability of the model to predict 3D simulation. Less than 10% simulation errors for k-ε and k-ω perhaps due to RANS is unable to predict the small unsteadiness in the wake, and this will cause a difference in the pressure drag [26], yet the results are within the acceptable range.

Table 4. Drag coefficient of Ahmed body.

Analysis	Experiment [24]	k-ε	k-ω	SA
C_D	0.286	0.3174	0.3023	0.34714
Error %	-	10.98	5.72	17.61

Qualitative: Velocity field

There are three locations to visualize the wake flow in the transverse direction, where plane A is located at z_A/L=-0.077, plane B is located at z_A/L=-0.19 and plane C is located at z_A/L=-0.479. The cross-field velocity distributions for our CFD model show good agreement with the experimental result for all three positions of transverse planes (refer to Figure 9 on page 24 in [24]. The velocity vector at plane A shown in Figure 11 presents the formation of side vortex, where the core is fed by the separation bubble, which is indicated by the low-pressure region. At plane B, Figure 12 shows that the separation bubble becomes smaller and the side edge vortex core is isolated at the top of the separation bubble. This indicates that the side edge vortex and upper separation bubble vortex merge together at first but are separated further downstream. Lastly, Figure 13 shows that the separation bubble is more pronounced, and the overall flow is dominated by the downwash vortices at plane C.

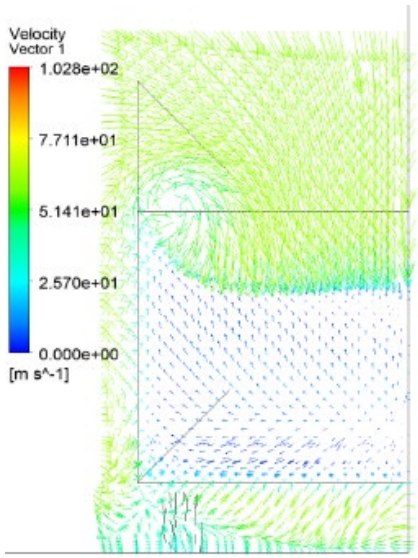

Figure 11. Cross field velocity distribution of Ahmed body at plane A in CFD simulation.

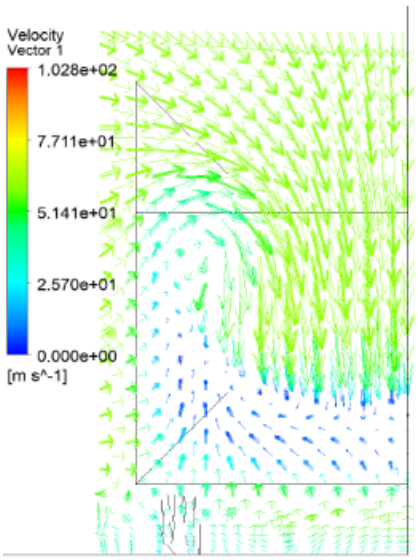

Figure 12. Cross field velocity distribution of Ahmed body at plane B in CFD simulation.

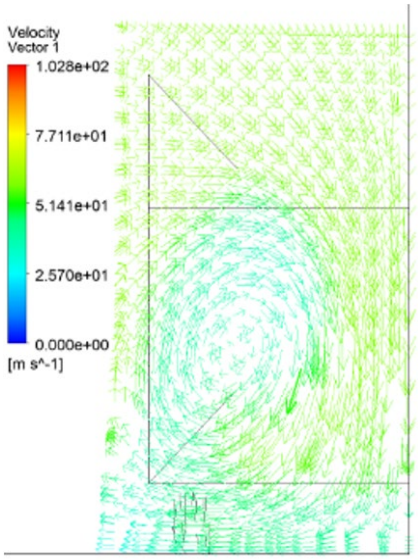

Figure 13. Cross field velocity distribution of Ahmed body at plane C in CFD simulation.

RESULTS AND DISCUSSION

Car Simulation

Lift and Drag Coefficients

Based on Table 5, the drag coefficient of the proposed Shell car is lower than the Ahmed body by about 61%. The former has a good aerodynamic performance for actual driving speeds (C_D=0.1216) with negative lift coefficients for better stability and traction.

Table 4. Aerodynamics Characteristics

Model	Re	C_L	C_D
Car	4.29×10^6	-0.03670	0.12500
	1.33×10^6	-0.02728	0.12160
Ahmed body	4.29×10^6	-	0.3166
	4.29×10^6 (experiment, [24])	-	0.2860

Qualitative contours and streamlines

It can be noticed from Figure 14(a) that a low pressure exists underneath the car-front. This might be due to the sudden change of flow direction from a curvy nose to its flat bottom. A small wake region is also formed behind the car in Figure 14(b), indicated by low-velocity navy blue zone. The top view pressure profile at Y=0.1m is shown in Figure 15 and the velocity profile is inversely proportional to that of the pressure and omitted for brevity. The airflow follows the shape of

the car smoothly and remains attached along the car body due to the streamline airfoil shape, as shown in Figure 16. This implies that the aerodynamic characteristic of a teardrop car (Shell car) is better than a blunt body (Ahmed body).

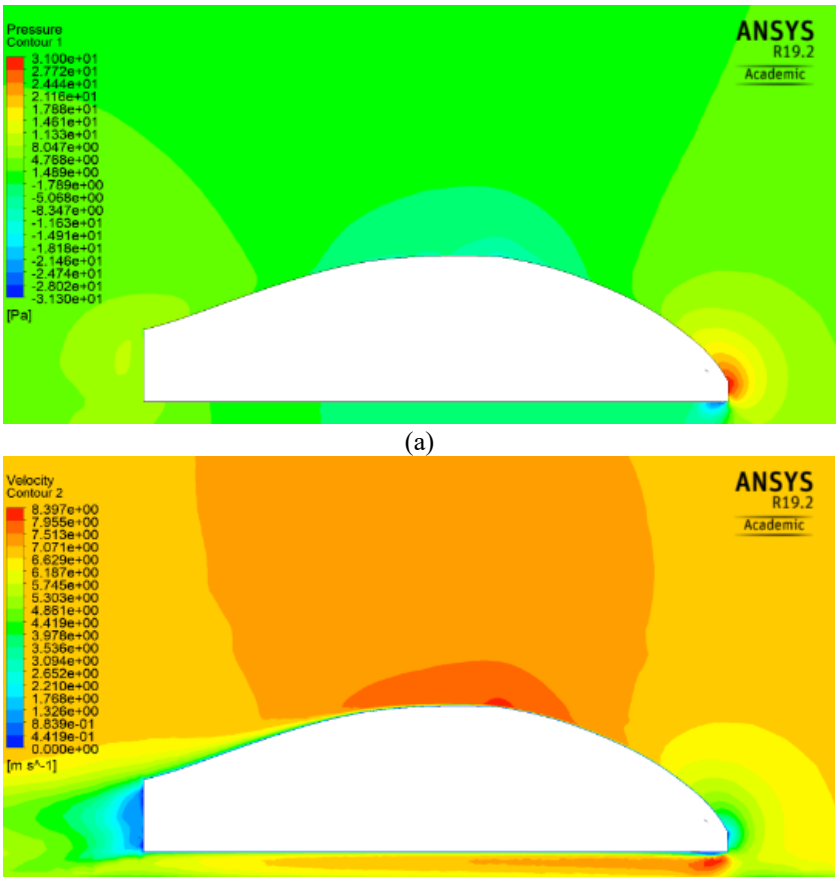

Figure 14. Side view (a) pressure contour (b) velocity contour of Shell car.

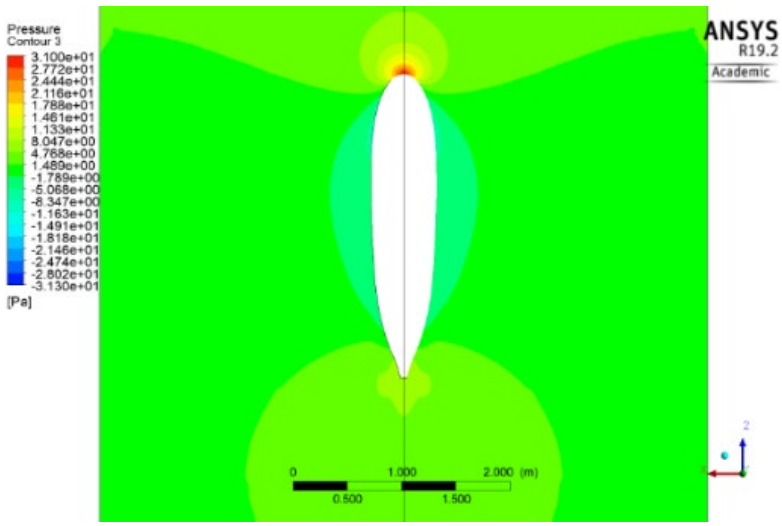

Figure 15. Top view pressure contour of Shell car.

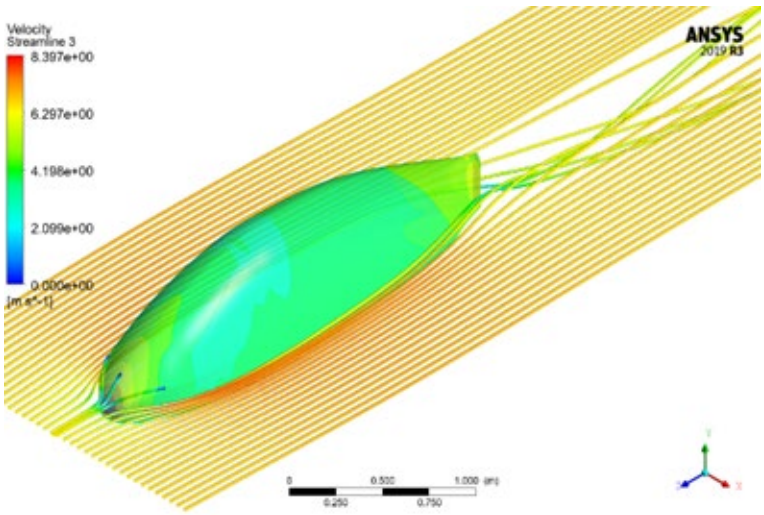

(a)

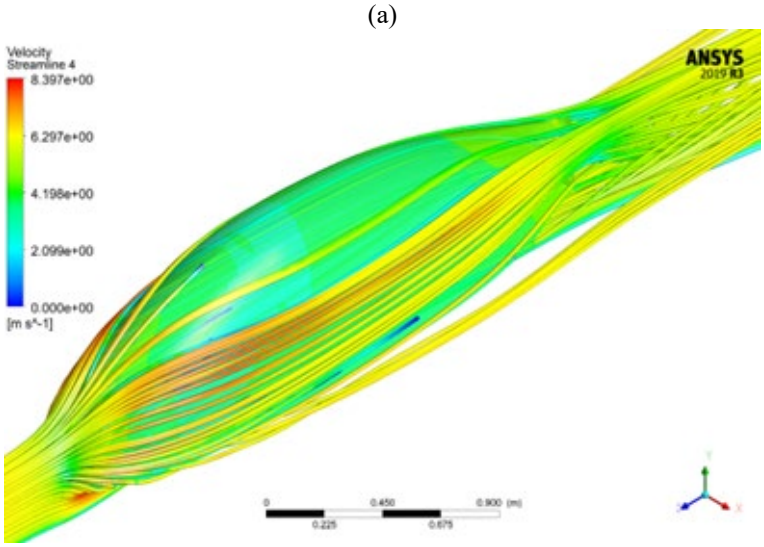

(b)

Figure 16. Streamline around Shell car at (a) Plane XZ=0.1m (b) full body.

Shape Optimization

There are many lengths, angles and heights variations done in this work on various parts of the Shell car, which includes the diffuser and stagnation point configurations. However, only the results of the two or three best configurations are reported herein.

Underbody Cut (Diffuser)

The underbody of the shell car is cut from the rear end with 17.86% (500 mm) and 25%(700 mm), which is relative to the car total length (of 2.8 m). This is also referred to as diffuser lengths in the paper. From Figure 17, C_D decreases when θ_d increases up to an optimum angle, then C_D increases and exceeds the result of base model at one point. The optimum diffuser angles are 15° and 10° and the optimum drag reduction are 7.9% and 10% for diffuser length of 17.86% and 25%, respectively. This demonstrates that a longer z_d/z_c (in percent) is more effective for drag reduction with smaller θ_d.

The results show that rear diffuser produces a downforce since C_L is more negative when θ_d increases, and this effect behaves inversely when the optimum angle is exceeded. It can be observed from Figure 18 that the desired low pressure at the underbody is created at the throat of the diffuser (as comparison with the base model) as airflow is accelerated through the region. However, the low-pressure bubble is reduced at higher θ_d thus, C_L is higher. The diffuser directs some airflow from the underbody to the low-pressure zone behind the car, smoothing the flow transition between the high-velocity airflow underneath the car and the much slower freestream airflow, in order to reduce the drag. However, this drag reduction effect is eliminated when the vortices at the wake are too strong.

Figure 18 and Figure 19 reveal that the pressure bubble behind the car is altered by the different θ_d. In general, the wake region behind Shell car is becoming smaller as θ_d increases up to an optimum angle, and after that, the wake region becomes larger as shown in Figure 20. Beyond an optimum angle, the flow is separated from the underbody cut due to the steep angle to form another wake region. However, there is exception for 25% z_d/z_c, where the flow is not separated at 15˚ although optimum angle is exceeded as shown in Figure 21. Two vortices are formed below the underbody cut

where a smaller vortex is formed on the top of the bigger vortex for both z_d/z_c. The vortices become larger and stronger in magnitude when θ_d increases.

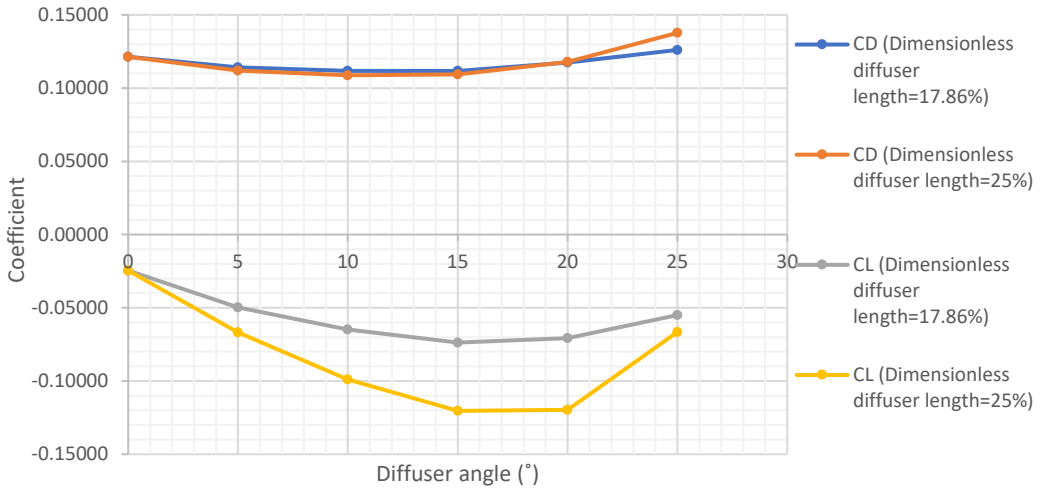

Figure 17. Aerodynamics coefficients vs diffuser angle for different diffuser length.

(a)

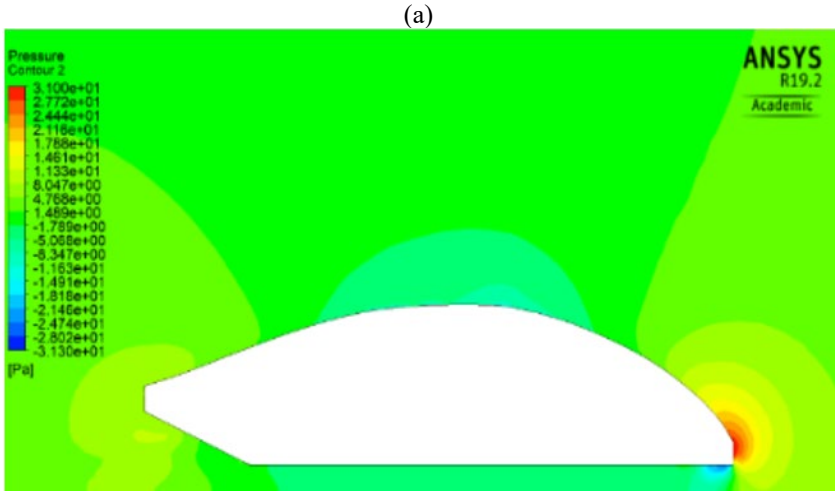

(b)

Figure 18. Side view pressure contour for 17.86% dimensionless diffuser length with (a) 15° (b) 25° diffuser angle.

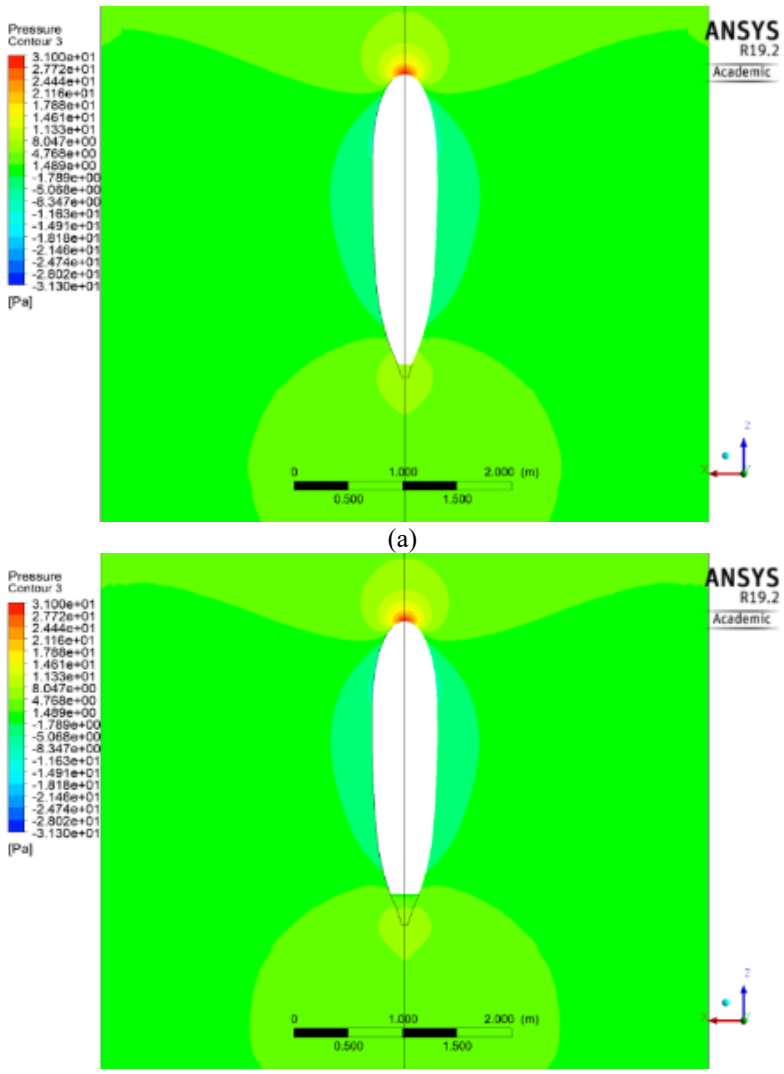

Figure 19. Top view pressure contour for 17.86% dimensionless diffuser length with (a) 15° and (b) 25° diffuser angle.

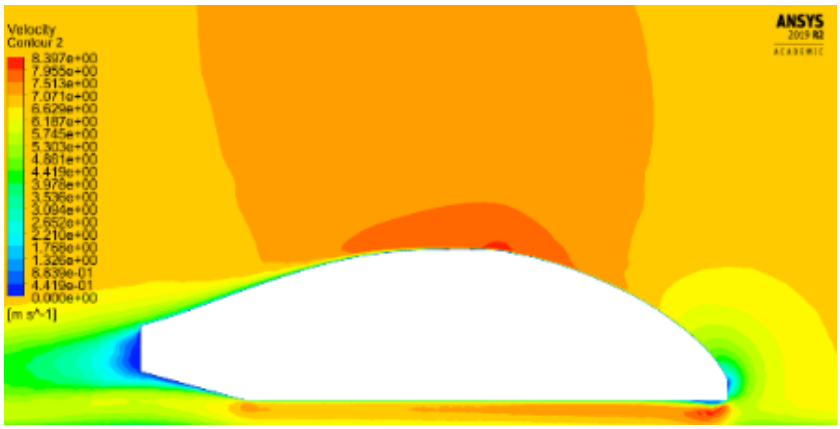

(b)

Figure 20. Side view velocity contour for 17.86% dimensionless diffuser length with (a) 15° and (b) 25° diffuser angle.

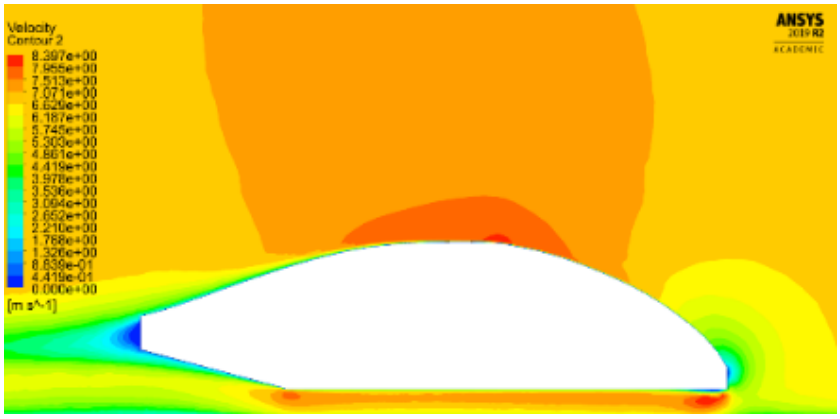

(a)

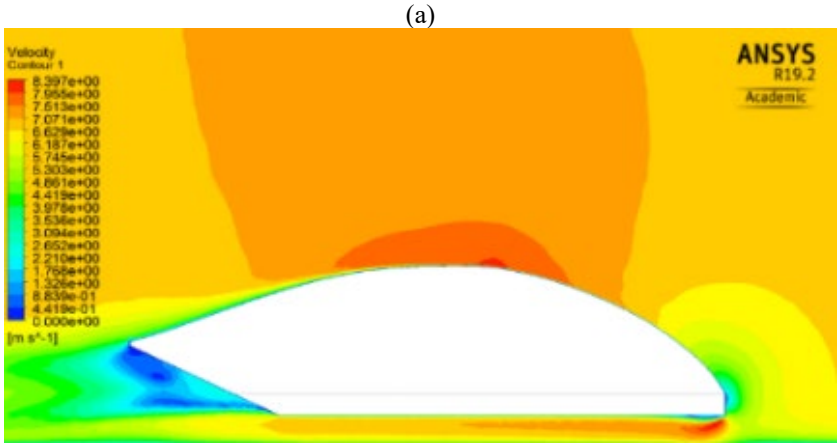

(b)

Figure 21. Side view velocity contour for 25% dimensionless diffuser length with (a) 15° and (b) 25° diffuser angle.

The shell car is further optimized with different dimensionless diffuser heights (relative to car height), 19.14% and 12.59%. Various dimensionless diffuser lengths (relative to car length) (10.71% ~ 25%) with constant y_d are investigated. Based on Figure 22, C_D decreases when z_d/z_c (in percent) increases for both y_d/y_c. The drag reduction does not significantly increase for higher z_d/z_c, and the highest drag reduction achieved is 10.3% and 9.2% for 19.14% and 12.59% y_d/y_c respectively. Other than that, the slope of C_D and C_L is steeper for greater y_d/y_c.

Based on Figure 23, the low-pressure bubble underneath the car is bigger for higher z_d/z_c thus C_L is decreasing. From Figure 24, the wake region behind the car becomes smaller when z_d/z_c increases because the flow separation underneath diffuser disappears. In overall, the influence of y_d on the drag reduction for different z_d/z_c is not significant.

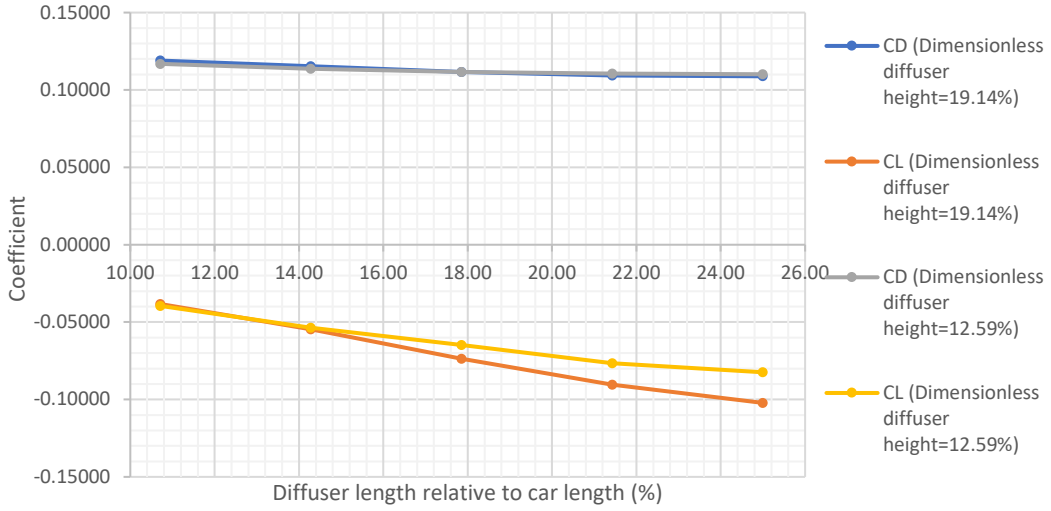

Figure 22. Aerodynamic Coefficients vs Diffuser length for different diffuser heights.

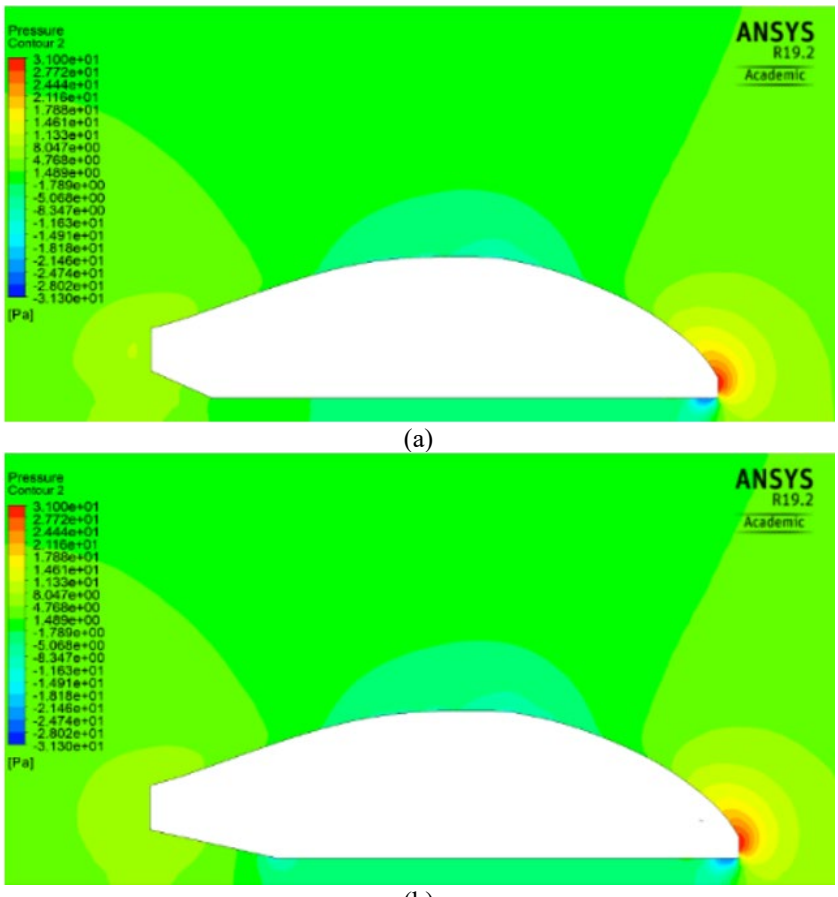

(a)

(b)

Figure 23. Pressure contour for 19.14% dimensionless diffuser height with (a) 10.71% (b) 21.43% dimensionless diffuser length.

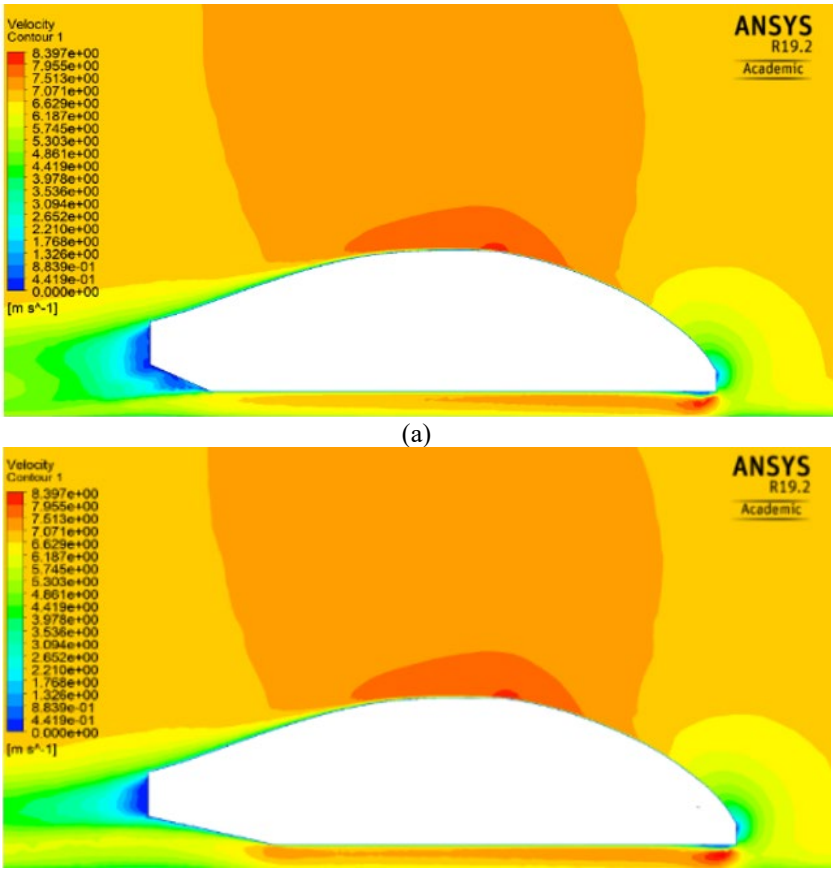

Figure 24. Velocity contour for 19.14% dimensionless diffuser height with (a) 10.71% (b) 21.43% dimensionless diffuser length.

The Shell car with diffuser angles of 15° and 10° are investigated for various dimensionless diffuser lengths (10.71% ~ 25%). Based on Figure 25, the trend of C_D and C_L is only slightly different with the case of diffuser heights, where the highest drag reduction achieved is 10.1% and 10.3% for 15° and 10° respectively. Based on Figure 26, the wake region becomes smaller when z_d/z_c increases, and the flow separation is smaller for lower θ_d. The effect of θ_d on the drag reduction for various z_d/z_c is not significant.

Different dimensionless stagnation point heights (relative to car height) of nose of Shell car are investigated with and without a diffuser (17.86% z_d/z_c and 15° θ_d). Based on Figure 27, the aerodynamics coefficient trend for both cases are almost similar. Firstly, the C_D is reduced as stagnation point height relative to car height (y_s/y_c) is increased until 14.29%. After that, the C_D increases until 21.43% of y_s/y_c, then decreases until 28.57% of y_s/y_c, and C_D goes up again until y_s/y_c reaches 42.86%. The lowest C_D are achieved at 28.57% and 14.29% of y_s/y_c respectively. The overall C_D with diffuser is lower than that without diffuser, but the drag reductions are significant even without diffuser, ranging from 13% to 17%. With the diffuser, a remarkable drag reduction of 23% can be achieved.

In general, the stagnation point height changes the pressure bubble distribution. From Figure 28, low-pressure bubbles at the underbody become smaller and the lift becomes more positive as y_s/y_c increases. Other than that, the high-pressure bubble at the car front gets smaller thus the pressure bubble is reduced up to 28.57%. Beyond that, the high-pressure bubbles become huge again. However, the distribution of the pressure bubble is changing inconsistently, especially at 28.57%, thus the profile of aerodynamics coefficients is not smooth. The high-velocity region indicated in red at the bottom of base model moves from car front to the highest point of the car shape, and it is bigger when y_s/y_c increases as shown in Figure 29.

When combined with a diffuser, the flow separation at the underbody cut occurs earlier and the wake region becomes bigger as y_s/y_c increases as shown in Figure 30. This is due to the increase of the underbody flow, which will increase the pressure gradient at the rear underbody to form adverse pressure gradients. Other than that, the diffuser is designed to increase the downforce by increasing the low-pressure bubble at the bottom, thus the overall C_L is lower than that without a diffuser as presented in Figure 31. Besides that, a diffuser reduces the pressure drag by smoothing the transition between the airflow at underbody and the low-pressure region behind the car (wake). In fact, the effect of diffuser on the pressure bubble will make some changes on the pressure distribution of different stagnation point heights.

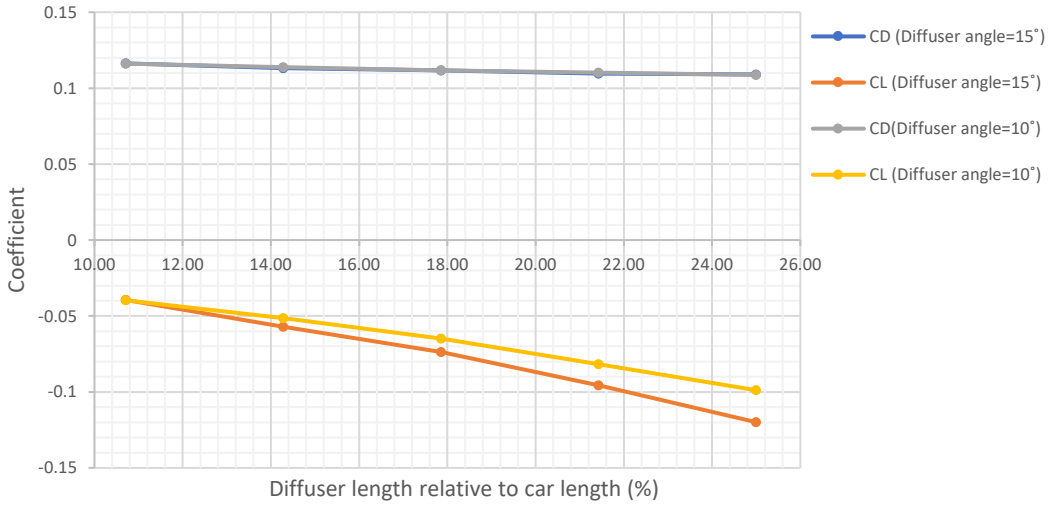

Figure 25. Aerodynamics coefficients vs diffuser length for different diffuser angle.

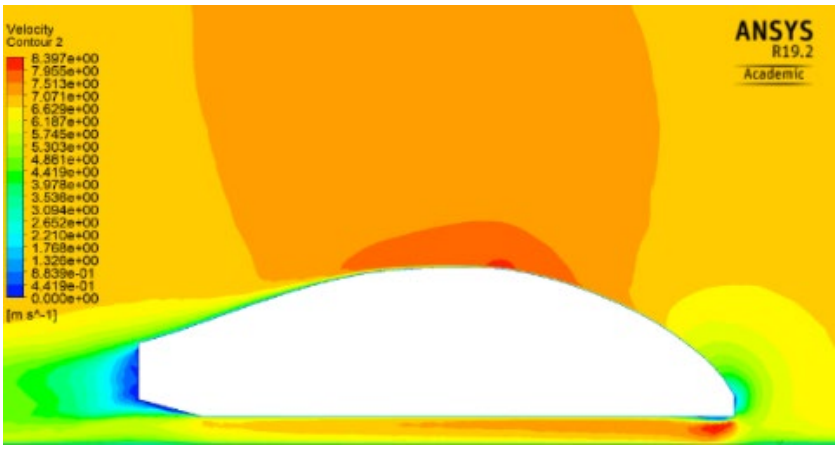

(a)

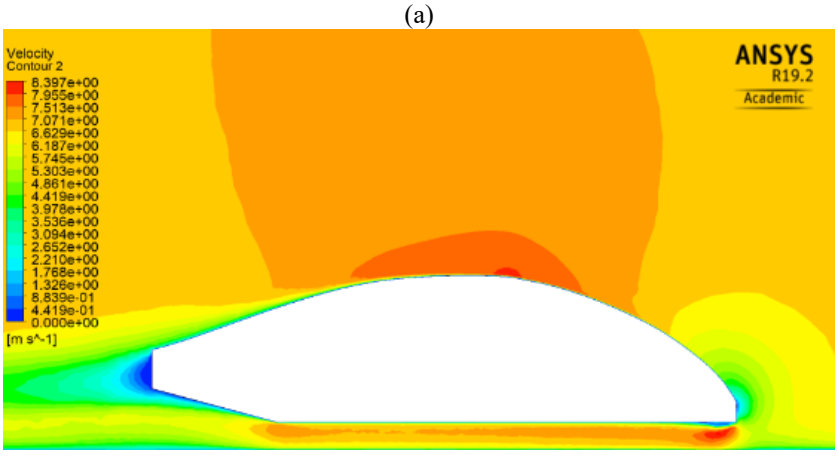

(b)

Figure 26. Velocity contour for 15° diffuser angle (a) 10.71% (b) 21.43% dimensionless diffuser length.

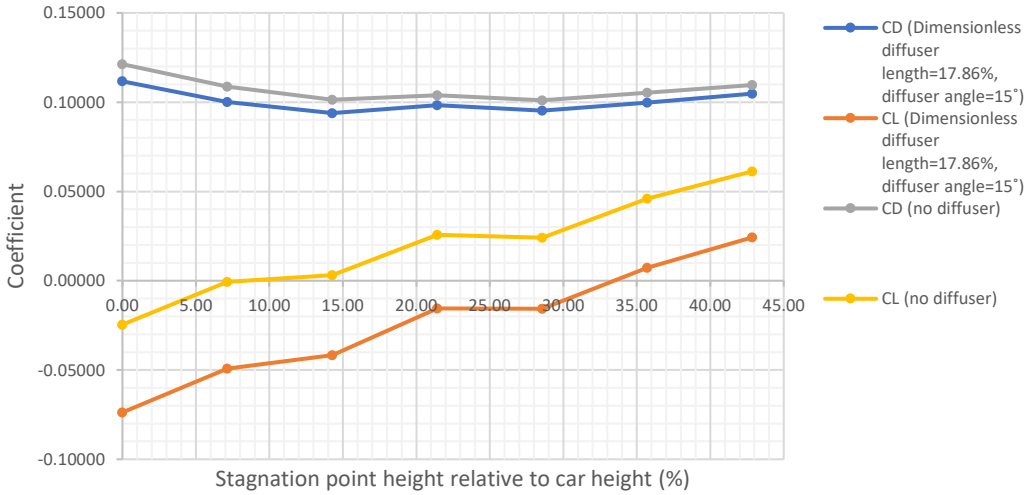

Figure 27. Aerodynamics coefficients vs stagnation point height.

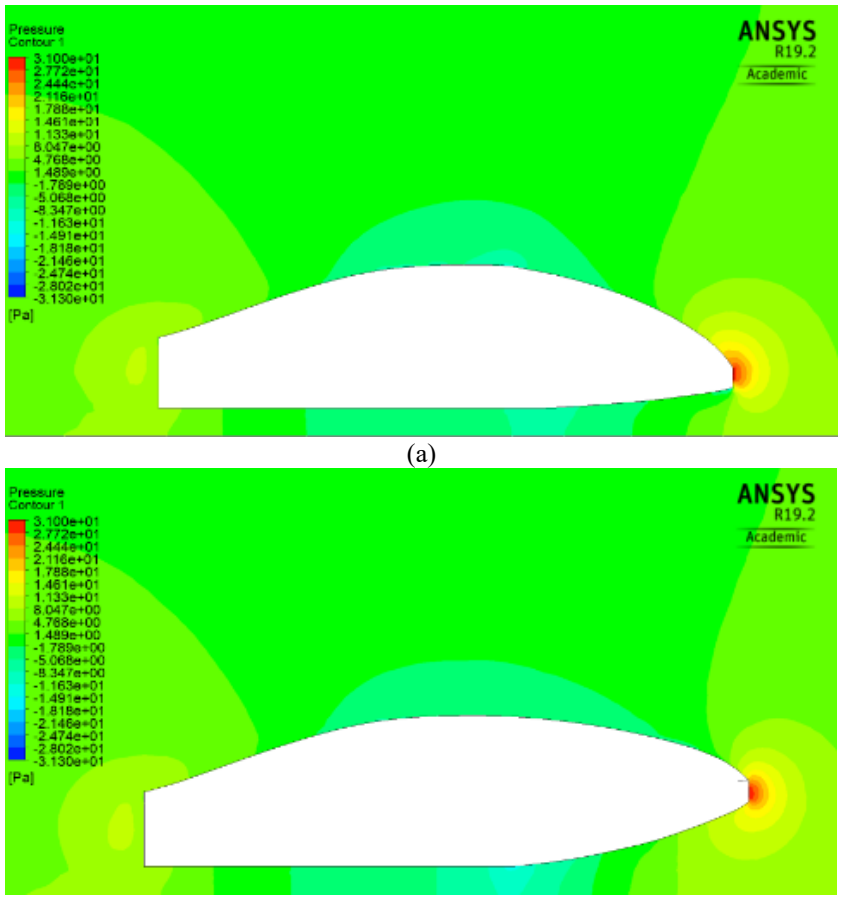

(a)

(b)

Figure 28. Pressure contour for (a) 14.29% (b) 35.71% dimensionless stagnation point height.

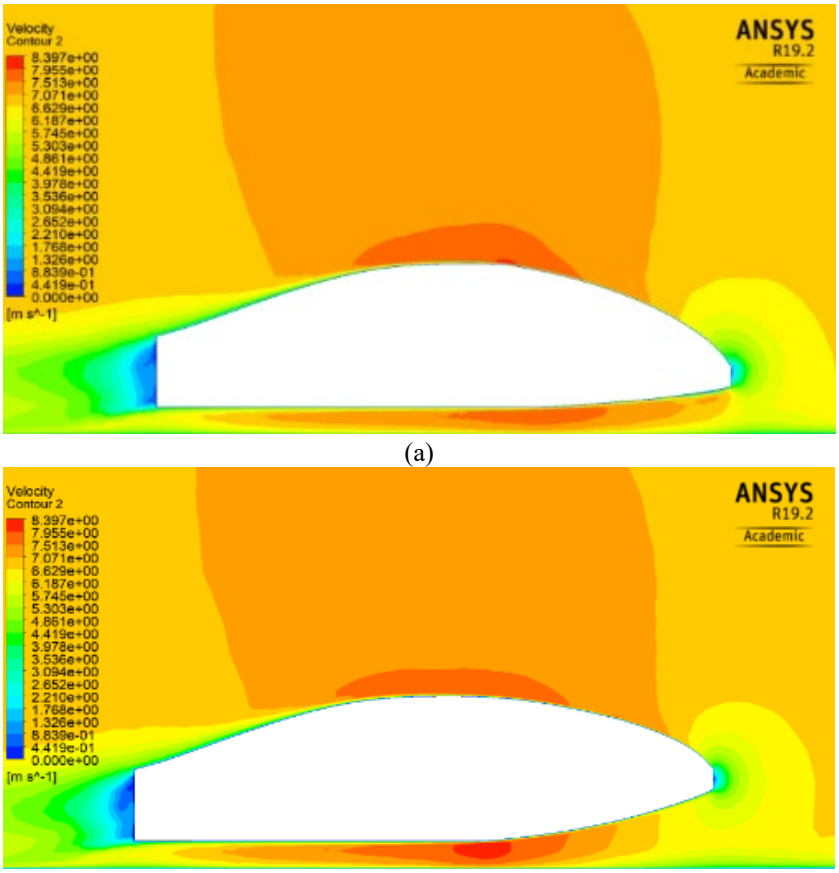

(a)

(b)

Figure 29. Velocity contour for (a) 14.29% (b) 35.71% dimensionless stagnation point height.

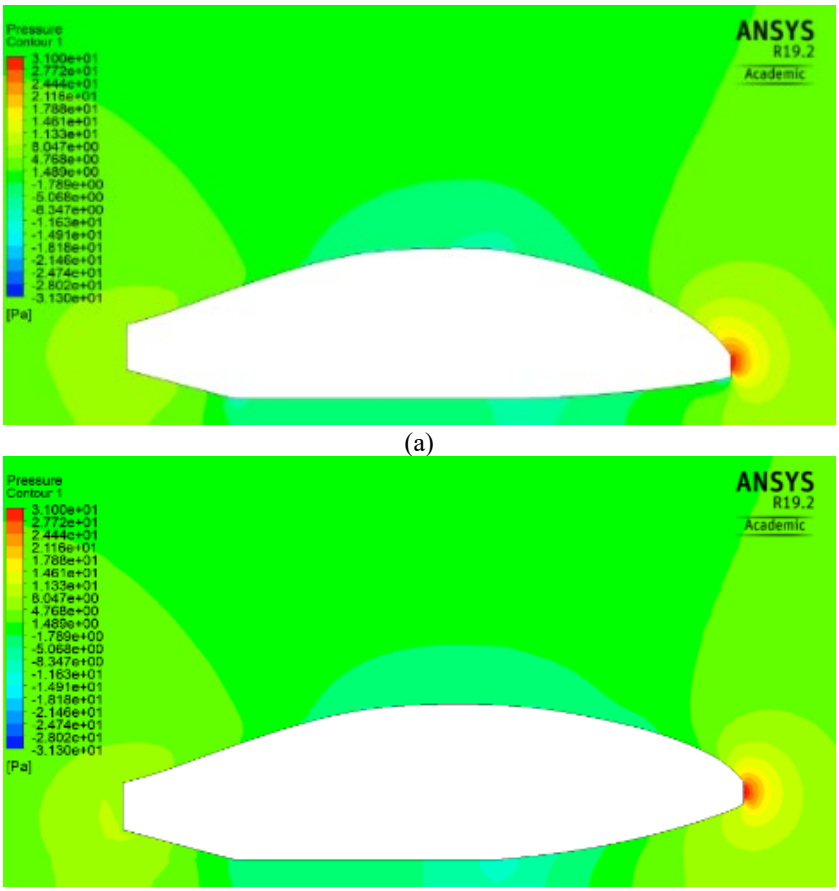

(a)

(b)

Figure 30. Pressure contour with diffuser for (a) 14.29% (b) 35.71% dimensionless stagnation point height.

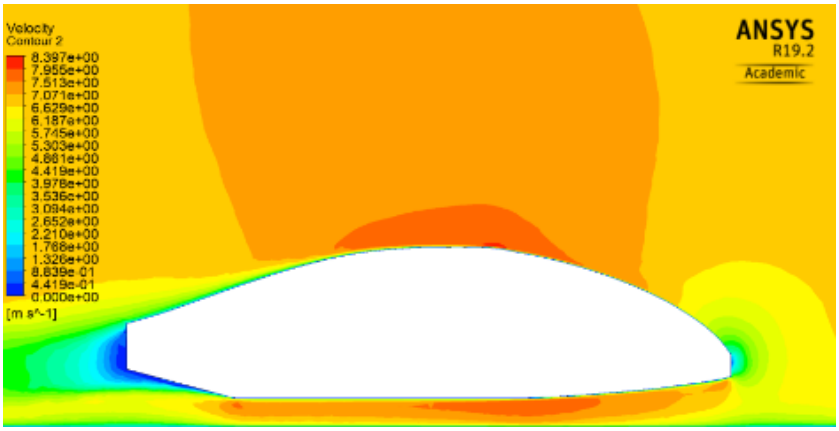

(a)

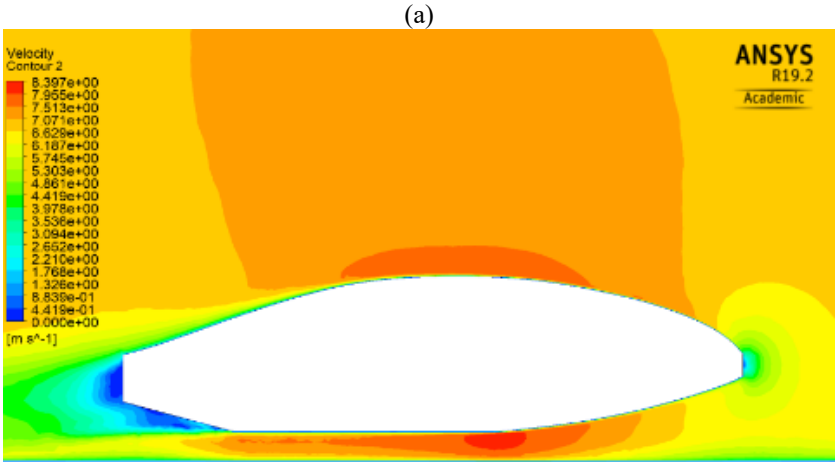

(b)

Figure 31. Velocity contour with diffuser for (a) 14.29% (b) 35.71% dimensionless stagnation point height.

CONCLUSION

The analysis of the aerodynamic performance of a fully-assembled Shell Eco-Marathon prototype car with a teardrop shape has been studied by the combined means of experiment and FVM numerical simulation. The aerodynamic investigation makes use of different parts of the car body including nose and rear underbody, to justify the aerodynamic contribution from the different body parts, including the contributions from the wake flow. Generally, it was found that the experimental findings [24] agree with the simulation data herein in terms of drag coefficient, with very little deviation being detected. The key findings results as follows:

i. The simulation results reveal that the teardrop shape of the Shell car body has a low C_D of 0.12. Rear underbody modifications alter the wake flow and together with the changes in stagnation point positions of the car can further improve the aerodynamics performance. There is an optimum diffuser angle where C_D is the minimum, and a longer diffuser length can produce a lower C_D.
ii. A drag reduction as high as 10.3% is achieved by using a diffuser with 25% dimensionless length and 10˚ angle. Isolated variations in diffuser heights and angles have only little influence on the drag.
iii. A higher $-\Delta C_D$ can be achieved by also changing stagnation point height, where the highest $-\Delta C_D$ of 25.1 % is achieved with 28.57% dimensionless height.
iv. The flow separation at the underbody cut occurs earlier and the wake region becomes bigger due to the increase of the underbody flow, which will increase the pressure gradient at the rear underbody to form adverse pressure gradients

ACKNOWLEDGEMENT

This work was supported by the Ministry of Education Malaysia for Fundamental Research Grant Scheme with Project Code: FRGS/1/2019/TK07/USM/02/3.

REFERENCES

[1] E. Guilmineau, "Computational study of flow around a simplified car body," *J. Wind Eng. Ind. Aerodyn.*, vol. 96, no. 6, pp. 1207–1217, 2008, doi: https://doi.org/10.1016/j.jweia.2007.06.041.
[2] M. Tientcheu-Nsiewe *et al.*, "Numerical study of a turbulent flow in the near-wake of an Ahmed body," *Am. J. Environ. Eng.*, vol. 2016, no. 6, pp. 157–163, 2016, doi: 10.5923/j.ajee.20160606.01.

[3] S. M. R. Hassan, T. Islam, M. Ali, and M. Q. Islam, "Numerical study on aerodynamic drag reduction of racing cars," *Procedia Eng.*, vol. 90, pp. 308–313, 2014, doi: https://doi.org/10.1016/j.proeng.2014.11.854.

[4] V. Sirenko, R. Pavlovs'ky, and U. S. Rohatgi, "Methods of reducing vehicle aerodynamic drag." In Proceedings of the ASME 2012 Fluids Engineering Division Summer Meeting collocated with the ASME 2012 Heat Transfer Summer Conference and the ASME 2012 10th International Conference on Nanochannels, Microchannels, and Minichannels, 2012. pp. 97-102. doi: 10.1115/FEDSM2012-72491.

[5] A. CifljDski, W. Prym, M. Stajuda, and D. Witkowski, "Investigation on aerodynamics of super effective car for drag reduction," *Mech. Mech. Eng.*, vol. 20, pp.295-308, 2016.

[6] J. J. Santin, *The world's most fuel efficient vehicle: Design and development of Pac Car II*. Zürich: vdf Hochschulverlag AG an der ETH Zürich, 2007.

[7] Umberto Ravelli, and Marco Savini, "Aerodynamic simulation of a 2017 F1 car with open-source CFD code," *J. Traffic Transp. Eng.*, vol. 6, no. 4, pp. 155–163, 2018, doi: 10.17265/2328-2142/2018.04.001.

[8] S. Thabet, and T. H. Thabit, "CFD simulation of the air flow around a car model (Ahmed Body)," *Int. J. Sci. Res. Publ.*, vol. 8, no. 7, pp. 517–525, 2018, doi: 10.29322/ijsrp.8.7.2018.p7979.

[9] Y. Haffner, J. Borée, A. Spohn, and T. Castelain, "Mechanics of bluff body drag reduction during transient near-wake reversals," *J. Fluid Mech.*, vol. 894, p. A14, 2020, doi: DOI: 10.1017/jfm.2020.275.

[10] H. Taiming, Z. Xiaodong, W. Zhongmin, and G. Zhengqi, "Experimental and numerical investigations of the vehicle aerodynamic drag with single-channel rear diffuser," *Proc. Inst. Mech. Eng. Part D J. Automob. Eng.*, vol. 234, no. 8, pp. 2216–2227, Feb. 2020, doi: 10.1177/0954407019893849.

[11] G. Pavia, M. A. Passmore, M. Varney, and G. Hodgson, "Salient three-dimensional features of the turbulent wake of a simplified square-back vehicle," *J. Fluid Mech.*, vol. 888, p. A33, 2020, doi: DOI: 10.1017/jfm.2020.71.

[12] D. E. Aljure, O. Lehmkuhl, I. Rodríguez, and A. Oliva, "Flow and turbulent structures around simplified car models," *Comput. Fluids*, vol. 96, pp. 122–135, 2014, doi: https://doi.org/10.1016/j.compfluid.2014.03.013.

[13] D. Barros *et al.*, "Bluff body drag manipulation using pulsed jets and Coanda effect," *J. Fluid Mech.*, vol. 805, pp. 422–459, 2016, doi: DOI: 10.1017/jfm.2016.508.

[14] M. Lorite-Díez *et al.*, "Drag reduction on a three-dimensional blunt body with different rear cavities under cross-wind conditions," *J. Wind Eng. Ind. Aerodyn.*, vol. 200, p. 104145, 2020, doi: https://doi.org/10.1016/j.jweia.2020.104145.

[15] C. R. Jadhav and R. P. Chorage, "Modification in commercial bus model to overcome aerodynamic drag effect by using CFD analysis," *Results Eng.*, vol. 6, p. 100091, 2020, doi: https://doi.org/10.1016/j.rineng.2019.100091.

[16] Y. Huang, S. Wang, Y. Ji, and Z. Liu, "Study of the automotive aerodynamic performance affected by entrance structure of forecabin," *Energy Built Environ.*, vol. 2, no. 3, pp. 327–335, 2021, doi: https://doi.org/10.1016/j.enbenv.2020.06.012.

[17] S. Maulenkul *et al.*, "An arbitrary hybrid turbulence modeling approach for efficient and accurate automotive aerodynamic analysis and design optimization," *Fluids* , vol. 6, no. 11. 2021, doi: 10.3390/fluids6110407.

[18] H. Chowdhury *et al.*, "Design of an energy efficient car by biomimicry of a boxfish," *Energy Procedia*, vol. 160, pp. 40–44, 2019, doi: https://doi.org/10.1016/j.egypro.2019.02.116.

[19] G. Franck, N. Nigro, M. Storti, and J. D'Elía, "Numerical simulation of the flow around the Ahmed vehicle model," *Lat. Am. Appl. Res.*, vol. 39, pp. 295–306, 2009.

[20] F. R. Menter, "Two-equation eddy-viscosity turbulence models for engineering applications," *AIAA J.*, vol. 32, no. 8, pp. 1598–1605, Aug. 1994, doi: 10.2514/3.12149.

[21] K. Oukassou, S. El, E. Mouhsine, and E. Hajjaji, "Comparison of the power, lift and drag coefficients of wind turbine blade from aerodynamics characteristics of Naca0012 and Naca2412," *Procedia Manuf.*, vol. 32, pp. 983–990, 2019, doi: 10.1016/j.promfg.2019.02.312.

[22] F. Ismail, P. M. Carrica, T. Xing, and F. Stern, "Evaluation of linear and nonlinear convection schemes on multidimensional non-orthogonal grids with applications to KVLCC2 tanker," *Int. J. Numer. Methods Fluids*, vol. 64, no. 8, pp. 850–886, Nov. 2010, doi: 10.1002/fld.2174.

[23] H. Chizari and F. Ismail, "Accuracy variations in residual distribution and finite volume methods on triangular grids," *Bull. Malaysian Math. Sci. Soc.*, vol. 40, no. 3, pp. 1231–1264, 2017, doi: 10.1007/s40840-015-0292-0.

[24] S. R. Ahmed, G. Ramm, and G. Faltin, "Some salient features of the time-averaged ground vehicle wake." SAE International, 1984, doi: https://doi.org/10.4271/840300.

[25] M. S. Abdullah, M. H. H. Ishak, and F. Ismail, "Numerical study of the 3D Savonius turbine under stationary conditions," *Eng. Fail. Anal.*, vol. 136, p. 106199, 2022.

[26] H. Lienhart, C. Stoots, and S. Becker, "Flow and turbulence structures in the wake of a simplified car model (Ahmed Model) in *New Results in Numerical and Experimental Fluid Mechanics III. Notes on Numerical Fluid Mechanics (NNFM)*, S. Wagner, U. Rist, H.J. Heinemann, R. Hilbig, Eds., Berlin: Springer, 2002, pp. 323–330.